

On multiscale quasi-interpolation of scattered scalar- and manifold-valued functions

Nir Sharon, Rafael Sherbu Cohen, Holger Wendland

Abstract

We address the problem of approximating an unknown function from its discrete samples given at arbitrarily scattered sites. This problem is essential in numerical sciences, where modern applications also highlight the need for a solution to the case of functions with manifold values. In this paper, we introduce and analyze a combination of kernel-based quasi-interpolation and multiscale approximations for both scalar- and manifold-valued functions. While quasi-interpolation provides a powerful tool for approximation problems if the data is defined on infinite grids, the situation is more complicated when it comes to scattered data. Hence, this paper is particularly interested in studying the improvement achieved by combining quasi-interpolation with a multiscale technique. The main contributions of this paper are as follows. First, we introduce the multiscale quasi-interpolation technique for scalar-valued functions. Second, we show how this technique can be carried over to the manifold-valued setting. Third, we give mathematical proof that converging quasi-interpolation will also lead to converging multiscale quasi-interpolation. Fourth, we provide ample numerical evidence that multiscale quasi-interpolation has superior convergence to quasi-interpolation. In addition, we will provide examples showing that the multiscale quasi-interpolation approach offers a powerful tool for many data analysis tasks, such as denoising and anomaly detection. It is especially attractive for cases of massive data points and high-dimensionality.

1 Introduction

We consider the problem of approximating an unknown function from its discrete samples. This classical problem is at the backbone of many scientific and engineering questions. For example, the samples could represent a physical quantity, a part of a biological system or a simulation process, and more. As it turns out, the scattered data sites, especially when dealing with a massive number of data points of high-dimensionality, make this reconstruction problem extremely challenging.

In this paper, we are interested in approximation methods which allow us to approximate not only scalar-valued functions but also functions which take their values in manifolds. We start by describing the former.

We define our scalar-valued approximation problem as follows. Let $X = \{x_j : j \in J\} \subseteq \Omega \subseteq \mathbb{R}^d$ be data sites and $\{v_j\}_{j \in J} \subseteq \mathbb{R}$ be the corresponding data values. Here, J is a possibly infinite index set and $\Omega \subseteq \mathbb{R}^d$ is the region of interest. We assume that the data values are samples, possibly in the presence of noise, of an unknown smooth enough function f , that is $v_j = f(x_j) + \varepsilon_j$, where ε_j is the noise term. Under these settings, a standard approach is to use a kernel $K: \Omega \times \Omega \rightarrow \mathbb{R}$ and its induced approximant,

$$s(x) = \sum_{j \in J} \alpha_j K(x, x_j), \quad x \in \Omega. \quad (1)$$

Often, the kernel is translation invariant or even radial, meaning it has the form $K(x, y) = \Phi(x - y) = \phi(\|x - y\|_2)$ with $\Phi: \mathbb{R}^d \rightarrow \mathbb{R}$ and $\phi: [0, \infty) \rightarrow \mathbb{R}$ and the $\|\cdot\|_2$ is the Euclidean norm in \mathbb{R}^d . Determining the coefficients α_j is then the main barrier in constructing the approximation.

A natural way to determine the coefficients of s of (1) is by interpolation, which requires s to satisfy $s(x_j) = v_j$, $j \in J$. This linear system is at the size of the number of data sites that fit inside the support of ϕ . Then, if this support is fixed and the number of data sites inside the support increases, the sequence of interpolants converges to the underline function. However, the interpolation matrices become denser and potentially more ill-conditioned, so computing and evaluating the interpolant becomes very expensive. Eventually, the advantage of compact support is lost. Conversely, if the support radius is chosen proportional to the data density, then the matrices are well-conditioned and sparse. Then, the evaluation is cheap, but there is no guarantee of convergence of the interpolant to f .

A remedy to this problem has been suggested in [14, 5], and the convergence has first been proven in [16, 32, 33, 51]. The idea is based on the assumption of a (possibly infinite) sequence of increasingly denser, usually nested, data sets X_1, X_2, \dots , and a simple residual correction scheme. The process starts when the target function is approximated on the coarsest grid X_1 . Next, the error of the first step is approximated on X_2 using a smaller support radius of ϕ and so on. This approach has not only the advantages of sparse, well-conditioned interpolation matrices in each step and fast, stable evaluations; it also allows us to capture different scales, if present, in the target function. We refer to this approach as *multiscale*. Other alluring computational alternative to interpolation is *quasi-interpolation*, where the coefficients of s of (1) are set as the values of samples, $\alpha_j = v_j$. The quasi-interpolation concept is used successfully in various areas and is well studied, particularly in spline spaces, see, e.g., [7, Chapter 12]. With suitable adjustments, these approximations introduce high-order accuracy, see, e.g., [13, 46].

Here, we suggest using quasi-interpolation in a residual correction scheme, that is, in a multiscale fashion. Our quasi-interpolation consists of a compactly supported radial basis function (RBF) [48]. So the resulted scheme provides an appealing computational technique to process massively large datasets in high dimensions. While similar approaches were studied numerically, in slightly different settings [12, 35], we suggest both numerical treatment and analytic consideration.

Manifold-valued functions are of the form $F: \Omega \rightarrow \mathcal{M}$, where \mathcal{M} is a Riemannian manifold. The simplicity and efficiency of the quasi-interpolation when equipped with a compactly supported Φ , makes this method particularly appealing for approximating manifold-valued functions, see, e.g., [18]. The manifold expresses both a global nonlinear structure together with local, constrained, high-dimensional elements. However, classical computational methods for approximation cannot cope with manifold-valued functions due to manifolds' non-linearity, and even fundamental tasks like integration, interpolation, and regression become challenging, see, e.g., [3, 28, 53].

The problem of approximating functions with manifold values has risen in various research areas, ranging from signal processing [4] and modern statistics [40] to essential applications such as brain networks and autism classification [52], structural dynamics and its application for aerodynamic problem solving [1, 34], to name a few. For example, in reduced-order models for simulations [2, 21] they drastically decrease the calculation time of simulating processes using interpolation of nonlinear structures at scattered locations and within high levels of accuracy [42].

In the paper, we show how to use our multiscale quasi-interpolation approach for manifold-values approximation based on the Riemannian center of mass. First, we provide a rigorous theoretical discussion, followed by a comprehensive numerical study that includes both the fine details of implementation together with an illustration of the multiscale approximation over scattered manifold data and its application. The alluring computational nature of the quasi-interpolation multiscale becomes even more essential for approximating manifold-values functions as the dimensionality and complexity of the manifold must be considered. In the numerical part, we provide comparison tests between the direct quasi-interpolation approximation and the multiscale approach and show its attractivity for an application of manifold-data processing.

The paper is organized as follows. Section 2 is dedicated to introducing essential notation, definitions, and background. In Section 3, we prove new error bounds for quasi-interpolation of scalar-valued functions. Then, Section 4 discusses the combination of quasi-interpolation and multiscale techniques in the scalar-valued setting. Here, we prove a very preliminary result, showing that multiscale quasi-interpolation converges at roughly the same rate as quasi-interpolation if the latter converges. In Section 5, we show how the construction of the multiscale quasi-interpolation method is formed for manifold data and provide the algorithm and a theoretical discussion. We summarize the manuscript with the numerical results given in Section 6. We first compare the performance of the multiscale quasi-interpolation to standard quasi-interpolation. Here, the numerical examples show two extraordinary features of multiscale quasi-interpolation. On the one hand, they show that non-converging quasi-interpolation can become convergent if combined with the multiscale technique. On the other hand, they show that the speed of convergence of quasi-interpolation can be improved by combining quasi-interpolation with the multiscale approach. There is some theoretical evidence for the first case in [15], though the situation described there does not apply to our scattered data problems and hence needs further theoretical backing. The same is true for the latter case. While it is easy to see that multiscale quasi-interpolation must converge if quasi-interpolation converges, see Section 4, there is still no rigorous proof for this yet. Finally, we study other aspects that highlight the advantages of the multiscale approach and present the multiscale approximation for manifold data, including its application for denoising a field of rotations contaminated with noise.

2 Preliminaries

We call an open, nonempty set $\Omega \subseteq \mathbb{R}^d$ a *domain*. Noting, however, that the term domain often also includes connectivity. We will look at classes of differentiable functions.

Definition 2.1. Let $\Omega \subseteq \mathbb{R}^d$ be a bounded domain. Let $k \in \mathbb{N}_0$. The spaces of k -times continuously differentiable functions are defined as

$$\begin{aligned} C^k(\Omega) &:= \{u: \Omega \rightarrow \mathbb{R} : D^\alpha u \in C(\Omega), |\alpha| \leq k\}, \\ C^k(\overline{\Omega}) &:= \{u \in C^k(\Omega) : D^\alpha u \text{ has a continuous extension to } \partial\Omega, |\alpha| \leq k\}. \end{aligned}$$

On the latter space we define the norm

$$\|u\|_{C^m(\overline{\Omega})} := \max_{|\alpha| \leq m} \sup_{x \in \overline{\Omega}} |D^\alpha u(x)|, \quad u \in C^m(\overline{\Omega}). \quad (2)$$

We will first collect the necessary material on quasi-interpolation. In the following, $\pi_m(\mathbb{R}^d)$ denotes the space of all d -variate polynomials of (total) degree less than or equal to $m \in \mathbb{N}_0$. For quasi-interpolation, we use the moving least squares method.

Definition 2.2. Let $X = \{x_1, \dots, x_N\} \subseteq \Omega \subseteq \mathbb{R}^d$ be given. Then, the *Moving Least-Squares* (MLS) approximation $Q_X(f)$ of degree $m \in \mathbb{N}_0$ to a function $f \in C(\Omega)$ is defined as follows. We choose *weight functions* $w_i: \Omega \rightarrow \mathbb{R}$, $1 \leq i \leq N$. For each $x \in \Omega$ we set $Q_X(f)(x) := p^*(x)$, where $p^* \in \pi_m(\mathbb{R}^d)$ is the solution of

$$\min \left\{ \sum_{i=1}^N |f(x_i) - p(x_i)|^2 w_i(x) : p \in \pi_m(\mathbb{R}^d) \right\}. \quad (3)$$

Next, we will assume that the weight functions $w_i: \Omega \rightarrow \mathbb{R}$ are compactly supported and introduce the index sets

$$I(x) := \{j \in \{1, \dots, N\} : w_j(x) \neq 0\}.$$

We present the quasi-interpolation operator and its polynomial reproduction property.

Definition 2.3. Let Q_X be a sample-based approximation functional of the form,

$$Q_X(f) = \sum_{i=1}^N f(x_i) a_i, \quad (4)$$

where a_i are weight functions. We say that Q_X *reproduces polynomials up to degree m* if for all $p \in \pi_m(\mathbb{R}^d)$, we have $Q_X(p) = p$, i.e.

$$p(x) = \sum_{i=1}^N p(x_i) a_i(x), \quad x \in \Omega. \quad (5)$$

Existence and certain properties of the MLS approximant are summarized in the following theorem. Its proof can be found, for example, in [50]. In its formulation we use the concept of $\pi_m(\mathbb{R}^d)$ -unisolvent sets. A set X is called $\pi_m(\mathbb{R}^d)$ -unisolvent, if the only function $p \in \pi_m(\mathbb{R}^d)$ that vanishes on all points from X is the zero function.

Theorem 2.4. Let $X = \{x_1, \dots, x_N\} \subseteq \Omega \subseteq \mathbb{R}^d$. Let $w_i \in C(\Omega)$, $1 \leq i \leq N$, be non-negative. Assume that for each $x \in \Omega$ the set $X(x) = \{x_i : i \in I(x)\}$ is $\pi_m(\mathbb{R}^d)$ -unisolvent. Then, the MLS approximation $Q_X(f)$ of (4) is well-defined for every $f \in C(\Omega)$, and it reproduces polynomial of degree m , see Definition 2.3. Moreover, there are unique functions a_1, \dots, a_N for (4), that can be written as

$$a_i(x) = w_i(x) \sum_{k=1}^Q \lambda_k(x) p_k(x_i), \quad 1 \leq i \leq N, \quad (6)$$

with a basis $\{p_1, \dots, p_Q\}$ of $\pi_m(\mathbb{R}^d)$ and certain values $\lambda_1(x), \dots, \lambda_Q(x)$, which are determined by the linear system

$$\sum_{k=1}^Q \left(\sum_{i=1}^N w_i(x) p_k(x_i) p_\ell(x_i) \right) \lambda_k(x) = p_\ell(x), \quad 1 \leq \ell \leq Q. \quad (7)$$

We will assume that the weight functions of (3) are of the form

$$w_i(x) = \Phi\left(\frac{x - x_i}{\delta_i}\right), \quad (8)$$

with a given function $\Phi : \mathbb{R}^d \rightarrow \mathbb{R}$. Typically, this function is either a *radial* function, i.e. a function of the form

$$\Phi(x) = \phi(\|x\|_2), \quad \phi : [0, \infty) \rightarrow \mathbb{R},$$

or of tensor product type, i.e.

$$\Phi(x) = \prod_{j=1}^d \phi_j(x_j), \quad \phi_j : \mathbb{R} \rightarrow \mathbb{R}.$$

For us this particular form is not important. We will, however, make the following assumption.

Assumption 2.5. For $X = \{x_1, \dots, x_N\}$ the weight functions $w_i : \mathbb{R}^d \rightarrow \mathbb{R}$ are given by (8) with $\delta_i > 0$ and a function $\Phi \in C^r(\mathbb{R}^d)$ having compact support $\text{supp } \Phi = \overline{\mathcal{B}(\mathbf{0}, 1)}$ and being positive on $\mathcal{B}(\mathbf{0}, 1) = \{x \in \mathbb{R}^d : \|x\|_2 < 1\}$.

If the data set X is chosen *quasi-uniform*, i.e. if the fill distance $h_{X,\Omega}$ and the separation radius q_X , given by

$$h_{X,\Omega} = \sup_{x \in \Omega} \min_{1 \leq j \leq N} \|x - x_j\|_2, \quad q_X = \frac{1}{2} \min_{j \neq k} \|x_j - x_k\|_2 \quad (9)$$

satisfy $q_X \leq h_{X,\Omega} \leq c_q q_X$ with a small constant $c_q \geq 1$ and if the radii are chosen proportional to $h_{X,\Omega}$, then the following crucial result holds.

Lemma 2.6. Let $X \subseteq \Omega$ be a quasi-uniform data set. Let the weights satisfy Assumption 2.5, where the support radii are chosen as $\delta_i = c_\delta h_{X,\Omega}$ with a sufficiently large constant $c_\delta > 0$. Then, the sets $X(x)$ are $\pi_m(\mathbb{R}^d)$ -unisolvent and the functions a_i from Theorem 2.4 belong to $C^r(\overline{\Omega})$ and satisfy

$$|D^\alpha a_i(x)| \leq C h_{X,\Omega}^{-|\alpha|}, \quad x \in \Omega, \quad 1 \leq i \leq N,$$

with a constant $C > 0$ independent of X , x and a_i .

Proof. This is proven in [38] and [39]. □

3 Error estimates for quasi-interpolation

We will now derive error estimates of the quasi-interpolation process, if the target functions are from $C^k(\overline{\Omega})$. The proofs are very similar to the proofs for Sobolev spaces in [38, 39].

Remark 3.1. In the following proof we require that the target function f is defined on the line connecting two arbitrary points $x, y \in \Omega$. This can be achieved by either assuming that Ω is convex or that f is defined on all of \mathbb{R}^d . The latter case is less relevant as we assume approximation operators with locality properties and hence we stick to convexity in the following theorem.

Recall that $m \in \mathbb{N}_0$ denotes the degree of the polynomials which are reproduced and that $r \in \mathbb{N}_0$ is the smoothness of the weights and $k \in \mathbb{N}$ is the smoothness of the target function.

Theorem 3.2. Let $\Omega \subseteq \mathbb{R}^d$ be a bounded, convex domain. Under all the above assumptions there is a constant $C > 0$ such that

$$\|f - Q_X(f)\|_{C^\ell(\overline{\Omega})} \leq C h_{X,\Omega}^{\min\{m+1, k\} - \ell} \|f\|_{C^{\min\{m+1, k\}}(\overline{\Omega})}$$

for all $f \in C^k(\mathbb{R}^d)$ and all $0 \leq \ell \leq \min\{r, m+1, k\}$.

Proof. As X is quasi-uniform, there is a constant $M > 0$ independent of N such that $\#I(x) \leq M$ for all $x \in \Omega$. This follows as usual from a geometric argument. We have $j \in I(x)$ if and only if $\|x - x_j\|_2 < \delta_j = c_\delta h_{X,\Omega} =: \delta$, i.e. if and only if $x_j \in \mathcal{B}(x, \delta)$. This implies

$$\bigcup_{j \in I(x)} \mathcal{B}(x_j, q_X) \subseteq \mathcal{B}(x, \delta + q_X),$$

and as the balls on the left-hand side are disjoint, we can conclude

$$\#I(x)q_X^d \leq (\delta + q_X)^d.$$

Quasi-uniformity $q_X \leq h_{X,\Omega} \leq c_q q_X$ then gives the upper bound

$$\#I(x) \leq \left(\frac{\delta}{q_X} + 1 \right)^d \leq (c_\delta c_q + 1)^d =: M.$$

Next, we use the notation $X(x) = \{x_j : j \in I(x)\}$. By the polynomial reproduction of the moving least-squares process, we have for any $p \in \pi_m(\mathbb{R}^d)$, any $\hat{x} \in \Omega$ and any $\alpha \in \mathbb{N}_0^d$ with $|\alpha| \leq \min\{r, k\}$,

$$\begin{aligned} |D^\alpha f(\hat{x}) - D^\alpha Q_X(f)(\hat{x})| &= |D^\alpha f(\hat{x}) - D^\alpha p(\hat{x}) + D^\alpha p(\hat{x}) - D^\alpha Q_X(f)(\hat{x})| \\ &\leq |D^\alpha f(\hat{x}) - D^\alpha p(\hat{x})| + \sum_{j \in I(\hat{x})} |D^\alpha a_j(\hat{x})| |p(x_j) - f(x_j)| \\ &\leq |D^\alpha f(\hat{x}) - D^\alpha p(\hat{x})| + \|f - p\|_{\ell_\infty(X(\hat{x}))} \left(1 + \sum_{j \in I(\hat{x})} C_\alpha h_{X,\Omega}^{-|\alpha|} \right) \\ &\leq |D^\alpha f(\hat{x}) - D^\alpha p(\hat{x})| + \|f - p\|_{\ell_\infty(X(\hat{x}))} (1 + C_\alpha M) h_{X,\Omega}^{-|\alpha|}. \end{aligned}$$

Next, we choose p as the Taylor polynomial $T_{\min\{m,k-1\}} f$ of f about \hat{x} , i.e.

$$p(x) = T_{\min\{m,k-1\}} f(x) = \sum_{|\beta| \leq \min\{m,k-1\}} \frac{D^\beta f(\hat{x})}{\beta!} (x - \hat{x})^\beta.$$

For $|\alpha| \leq \min\{m, k-1\}$, it is well-known and shown by a straight-forward calculation that

$$D^\alpha T_{\min\{m,k-1\}} f = T_{\min\{m,k-1\}-|\alpha|} D^\alpha f.$$

This immediately shows for $|\alpha| \leq \min\{m, k-1\}$ that $D^\alpha f(\hat{x}) = D^\alpha p(\hat{x})$ holds. Moreover, as Ω is convex, we can use the Lagrange remainder formula in the form

$$f(x) - p(x) = \sum_{|\beta| = \min\{m+1,k\}} \frac{D^\beta f(\xi)}{\beta!} (x - \hat{x})^\beta,$$

with ξ on the line connecting x and \hat{x} . This shows for $x \in X(\hat{x})$, the bound

$$|f(x) - p(x)| \leq C \delta^{\min\{m+1,k\}} \|f\|_{C^{\min\{m+1,k\}}(\bar{\Omega})}.$$

Combining this with the estimate above, we find for $|\alpha| \leq \min\{r, m, k-1\}$,

$$\|D^\alpha f - D^\alpha Q_X(f)\|_{C(\bar{\Omega})} \leq C h_{X,\Omega}^{\min\{m+1,k\}-|\alpha|} \|f\|_{C^{\min\{m+1,k\}}(\bar{\Omega})}. \quad (10)$$

We finally need to extend this bound to the situation of $|\alpha| \leq \min\{r, m+1, k\}$. Hence, we only have to show something in addition if $\min\{m+1, k\} \leq r$. In this case, we have for the Taylor polynomial $p = T_{\min\{m,k-1\}}$ and $|\alpha| = \min\{m+1, k\} = \min\{m, k-1\} + 1$ obviously $D^\alpha p(\hat{x}) = 0$. This then shows

$$|D^\alpha f(\hat{x}) - D^\alpha Q_X(f)(\hat{x})| \leq |D^\alpha f(\hat{x})| \leq \|f\|_{C^{\min\{m+1,k\}}(\bar{\Omega})},$$

which is the desired extension of (10). □

Obviously, it makes sense to align the three parameters m, k, r as follows.

Corollary 3.3. *If the smoothnesses are chosen as $k = r = m + 1$ then,*

$$\|f - Q_X(f)\|_{C^\ell(\bar{\Omega})} \leq C_{k,\ell} h_{X,\Omega}^{k-\ell} \|f\|_{C^k(\bar{\Omega})}, \quad (11)$$

for all $f \in C^k(\bar{\Omega})$ and all $0 \leq \ell \leq k$.

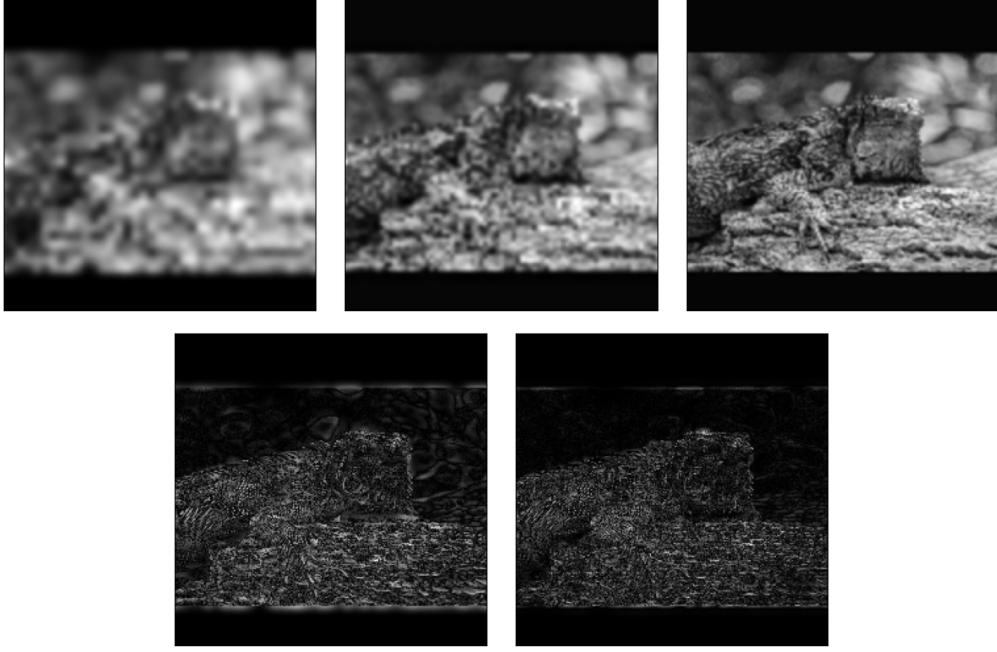


Figure 1: An illustrative example of multiscale approximation of an iguana photo, taken by H R from Pexels. The upper row is the approximation in different levels. The lower row is the error of the previous iteration. To calculate the next iteration, we approximate the error and add it to the previous approximation. We use a quasi-interpolation of the form (4) with $\sum_i a_i = 1$ (Shepard's method), scaling factor of $\mu = 0.5$, and the sample fill distance is $h_X = 0.008$. For more details see Section 6.

4 Multiscale based on quasi-interpolation

This section introduces our multiscale approach via our error correction transform. We begin by presenting the setup. Then, we provide the algorithm and a first illustrative example. Finally, we use the above error estimates to derive a convergence result for our multiscale scheme based on quasi-interpolation approximation.

A multiscale approximation is an iterative approach that combines trends from different scales of the approximated functions. We start from the approximation of low-resolution samples of the function. Then, each consecutive iteration approximates the error of the previous iteration with samples of higher resolution and uses the result to improve the previous approximant.

Here, the general set-up is as follows. We have a sequence of data sets $X_1, X_2, \dots \subseteq \Omega$ with mesh norms $h_j = h_{X_j, \Omega}$, which are monotonically decreasing. To ensure a certain uniformity in decrease, we will assume that $h_{j+1} = \mu h_j$ for some fixed *scaling factor* $\mu \in (0, 1)$. We will also require that the sequence is *quasi-uniform*, which means that there is a constant c_q such that, with $q_j = q_{X_j}$,

$$q_j \leq h_j \leq c_q q_j.$$

Next, we will pick a support radius for each level as $\delta_j = \nu h_j$ with a fixed $\nu > 1$ and form moving least-squares approximation operators for level j based on the points in $X_j = \{x_1^{(j)}, \dots, x_{N_j}^{(j)}\}$ as

$$Q_j f := \sum_{i=1}^{N_j} f(x_i^{(j)}) a_i^{(j)},$$

where the $a_i^{(j)}$ are built using the weights

$$w_i^{(j)}(x) = \Phi \left(\frac{x - x_i^{(j)}}{\delta_j} \right),$$

with a compactly supported function $\Phi: \mathbb{R}^d \rightarrow \mathbb{R}$ as before.

The multiscale quasi-interpolation algorithm then works as a standard residual correction algorithm, as detailed in Algorithm 1. We provide in Figure 1 an illustrative example of applying our residual correction algorithm for the approximation of an image.

Algorithm 1 Multiscale quasi-interpolation

Input: function to approximate f , levels number n , sequence of data sets $X_0, \dots, X_{n-1} \subseteq \Omega$

Output: The approximation of f , that is f_n

$f_0 = 0, e_0 = f$

for $j = 1, 2, \dots, n$ **do**

 Compute the quasi-interpolation $s_j = Q_j e_{j-1}$ to e_{j-1} based on data over X_{j-1}

$f_j = f_{j-1} + s_j$

$e_j = e_{j-1} - s_j$

end for

With this at hand, we have the following convergence result for our multiscale quasi-interpolation approximation.

Theorem 4.1. *Let $\Omega \subseteq \mathbb{R}^d$ be a convex, bounded domain. Let $X_j \subseteq \Omega$ be a sequence of quasi-uniform data sets with fill-distances $h_{j+1} = \mu h_j$, $\mu \in (0, 1)$. Let $\delta_j = \nu h_j$ with $\nu > 1$. Let $\Phi \in C^k(\bar{\Omega})$, $k \in \mathbb{N}$, and let the moving quasi-interpolation approximation reproduce polynomials of degree $m \geq k - 1$. Then, there is a constant $C > 0$ such that*

$$\|f - f_n\|_{C^k(\bar{\Omega})} \leq C_{0,k} (C_{k,k} \mu^k)^n \|f\|_{C^k(\bar{\Omega})}, \quad (12)$$

where the constants are from Corollary 3.3. Hence, the method converges if we choose μ such that $C_{k,k} \mu^k < 1$.

Proof. By Corollary 3.3, we have with $\ell = k$,

$$\|e_j\|_{C^k(\bar{\Omega})} = \|e_{j-1} - Q_j e_{j-1}\|_{C^k(\bar{\Omega})} \leq C_{k,k} \|e_{j-1}\|_{C^k(\bar{\Omega})}, \quad 1 \leq j \leq n.$$

Iterating this leads to the bound

$$\|e_n\|_{C^k(\bar{\Omega})} \leq C_{k,k}^n \|e_0\|_{C^k(\bar{\Omega})} = C_{k,k}^n \|f\|_{C^k(\bar{\Omega})}.$$

Applying Corollary 3.3 with $\ell = 0$ then yields

$$\begin{aligned} \|e_n\|_{C(\bar{\Omega})} &= \|Q_{X_n}(e_{n-1}) - e_{n-1}\| \leq C_{0,k} h_n^k \|e_{n-1}\|_{C^k(\bar{\Omega})} \\ &\leq C_{0,k} h_n^k C_{k,k}^n \|f\|_{C^k(\bar{\Omega})} \leq C_{0,k} (\mu^k C_{k,k})^n \|f\|_{C^k(\bar{\Omega})}. \end{aligned}$$

□

Note that the convergence enforcing term $(C_{k,k} \mu^k)^n$ contains in particular $\mu^{kn} = h_n^k$ which coincides with the convergence enforcing term for the standard quasi-interpolation scheme. Here, however, we also have the additional factor $C_{k,k}^n$. If $C_{k,k} > 1$ this would reduce the convergence significantly. If, however, $C_{k,k} < 1$, we would have improved convergence. Unfortunately, the constant $C_{k,k}$ is not really accessible and also depends on the factor $\nu > 1$ from $\delta_j = \nu h_j$. Though, it might be possible to enforce a small $C_{k,k}$ by choosing ν wisely, a simple calculation in the case $k = 1$ shows that the above mathematical techniques always lead to a constant $C_{1,1} > 1$ which can become arbitrarily close to 1 by increasing ν . Nonetheless, the numerical examples below show that these mathematical techniques do not truly reflect the error behaviour of the multilevel quasi-interpolation scheme. Obviously, more research in this direction is necessary.

5 Transition to the setting of manifold-valued data

In this section we construct the theory for quasi-interpolation and multiscale approximation for manifold-valued functions. We begin with changing notations for manifolds. Then, we show how the moving least squares method is translated to manifold-valued data via the Karcher mean. After that, we define the smoothness descriptor which is the manifold version of C^k . We end with the quasi-interpolation and multiscale versions and results that we do not prove.

5.1 Updating our notation

Let \mathcal{M} be a Riemannian manifold equipped with Riemannian metric which we denote by $\langle \cdot, \cdot \rangle$. The Riemannian geodesic distance $\rho(\cdot, \cdot): \mathcal{M}^2 \rightarrow \mathbb{R}_+$ is

$$\rho(b, q) = \inf_{\Gamma} \int_0^1 |\dot{\Gamma}(t)| dt, \quad (13)$$

where $\Gamma: [0, 1] \rightarrow \mathcal{M}$ is a curve connecting points $\Gamma(0) = b$ and $\Gamma(1) = q$, and $|\cdot|^2 = \langle \cdot, \cdot \rangle$.

Manifold-valued functions map a Euclidean domain Ω to a fixed, known manifold \mathcal{M} . We denote manifold-valued functions with uppercase letters and functions with vector values, such as values from a tangent space of \mathcal{M} , in lowercase letters. Also, denote the exponential map of a vector v in the tangent space $T_{\mathcal{M}}(b)$ around a base point b , and its inverse logarithm map by

$$b \oplus v = \text{Exp}_b(v), \quad \text{and} \quad q \ominus b = \text{Log}_b(q), \quad b, q \in \mathcal{M}.$$

Namely, $b \oplus v$ maps a vector v at $T_{\mathcal{M}}(b)$ to the point on the manifold which lies at a distance $\|v\|$ along the geodesic line from b parallel to v . If q is inside the injectivity radius, then $b \oplus (q \ominus b) = q$ and the geodesic distance $\rho(b, q)$ is merely $\|q \ominus b\|$, with the Euclidean norm at $T_{\mathcal{M}}(b)$. When G and H are \mathcal{M} -valued functions (or sequences), we assume a common representation (or indexing), for example, $G \ominus H = G(x) \ominus H(x)$ for all x in the common domain.

5.2 Applying Karcher means

We generalize the quasi-interpolation scheme (4) to manifold-valued scattered data, based on the given Riemannian structure, via the notion of Karcher mean. This intrinsic averaging method adapts scalar operators to manifold values and naturally agrees with the quasi-interpolation MLS formulation (3) as we will see next.

We refer to the linear combination at (4) and assume that the coefficients form a partition of unity, that is they satisfy

$$\sum_{i=1}^N a_i(x) = 1, \quad x \in \Omega.$$

This condition implies the exact reproduction of constants, see Definition 2.3. More details on such operators are given on Section 6. Next, for any x , the value in (4) can be characterized as the unique solution of the optimization problem

$$\arg \min_{y \in \mathbb{R}} \sum_{i=1}^N a_i \|y - f(x_i)\|^2. \quad (14)$$

Namely, this form identifies the linear combination (4) as the Euclidean center of mass. In particular, the result of (14) is the center of mass of $\{f(x_i)\}_{i=1}^N$ with respect to the weights $\{a_i\}_{i=1}^N$.

For \mathcal{M} -valued data, we rewrite the optimization problem (14) by replacing the Euclidean distance with the Riemannian geodesic distance (13) and restrict the search space to our manifold. Namely, for the samples of a manifold-valued function F we define,

$$Q_X^{\mathcal{M}}(F)(x) = \arg \min_{q \in \mathcal{M}} \sum_{i=1}^N a_i \rho(q, F(x_i))^2, \quad x \in \Omega. \quad (15)$$

The above is the manifold-valued counterpart of the approximation operator Q from (4) for constant reproduction. We focus on cases when the solution of (15) exists uniquely and then it is termed the *Riemannian center of mass* [20]. The solution of (15) is also known as Karcher mean (especially for matrices) and Fréchet mean in general metric spaces, see [30]. The global well-definedness of (15) when $a_i \geq 0$ is studied in [31]. Moreover, when \mathcal{M} has a non-positive sectional curvature, a globally unique solution for (15) can be found, see e.g., [23, 29, 43]. Recent studies of manifolds with positive sectional curvature show necessary conditions for uniqueness on the spread of points with respect to the injectivity radius of \mathcal{M} [9, 25]. Note that one may interpret many alternative methods for adapting approximation operators to manifold values as finite approximations for the Riemannian center of mass (15). The finiteness implies that one usually does not have direct access to the Riemannian center of mass and thus must apply an iterative process for calculating it. Finite procedures include, for example, exp-log methods [19, 41], repeated binary averaging [10, 45], inductive means [11], and more. Next, in the numerical section, we show examples of algorithms for calculating the Karcher mean.

5.3 Smoothness descriptor

For obtaining error bounds, we must first show how we measure the smoothness of a manifold-valued function. In other words, we seek manifold-valued settings analogous to the spaces of k -times continuously differentiable functions and their norms. One natural generalization uses smoothness descriptors [17, 18]. Specifically, we are inspired by [18] where the smoothness descriptor uses the covariant derivatives of a manifold-valued function $F : \Omega \rightarrow \mathcal{M}$. In our analysis, we examine the deviation between F and its approximation $Q_X^{\mathcal{M}}(F)$, that is $F \ominus Q_X^{\mathcal{M}}(F)$. This quantity is a vector field attached to $Q_X^{\mathcal{M}}(F)$ and therefore, the smoothness descriptor we present is given as the C^k norm of a vector field.

Let $G : \Omega \rightarrow \mathcal{M}$ be a function with a vector field W attached to it. That is, for all $x \in \Omega$, $W(x) \in T_{G(x)}\mathcal{M}$. Then, the r -th index of the covariant derivative of W in the direction x^l is given by

$$\frac{D}{dx^l} W^r(x) := \frac{dW^r}{dx^l}(x) + \Gamma_{ij}^r(G(x)) \frac{dG^i}{dx^l} W^j(x), \quad (16)$$

where we sum over repeated indices and denote with Γ_{ij}^r the Christoffel symbols associated to the metric of \mathcal{M} as in [8]. In addition, W^i and G^i mean the i -th component of W and G , respectively.

For iterated covariant derivatives we introduce the symbol $\mathcal{D}^{\mathbf{l}}(F \ominus G)$ which means covariant partial differentiation along $F \ominus G$ with respect to the multi-index \mathbf{l} in the sense that

$$\mathcal{D}^{\mathbf{l}}(F \ominus G) := \frac{D}{dx^{l_k}} \cdots \frac{D}{dx^{l_1}}(F \ominus G).$$

All derivatives are vector fields attached to G . We finally define the vector field smoothness descriptor of the error $F \ominus G$, which is the manifold analogue of (2).

Definition 5.1. For functions $F, G : \Omega \rightarrow \mathcal{M}$, and $U \subseteq \Omega$, we define the k -th order smoothness descriptor:

$$\|F \ominus G\|_{C^k(\bar{U})} := \max_{|\mathbf{l}| \leq k} \sup_{x \in U} \left| \mathcal{D}^{\mathbf{l}}(F \ominus G) \right|_{g(G(x))},$$

where g is the metric tensor of \mathcal{M} , and it induces the metric $|\cdot|_{g(p)}$ on the tangent space $T_p\mathcal{M}$ at $p \in \mathcal{M}$.

Following the last definition, we further define the induced smoothness class:

Definition 5.2. We say that a function $F : \Omega \rightarrow \mathcal{M}$ is locally in $C^k(p, \bar{\Omega})$, with respect to a fixed point $p \in \mathcal{M}$, if $\|F \ominus B\|_{C^k(\bar{U})}$ is finite inside the ball around p within the injectivity radius. If, in addition, $F \in C^k(p, \bar{\Omega})$ for any $p \in \mathcal{M}$ we say that $f \in C^k(\bar{\Omega})$.

Given a function $F \in C^k(\bar{\Omega})$, we wish for a manifold analogue of (11), that is, a bound of the form

$$\left\| F \ominus Q^{\mathcal{M}}(F) \right\|_{C^\ell(\bar{\Omega})} \leq C_{k,\ell} h_{X,\Omega}^{k-\ell} \|F \ominus B\|_{C^k(\bar{\Omega})}, \quad (17)$$

where $B : \Omega \rightarrow \mathcal{M}$ is a reference function such that $B(x)$ is within the injectivity radius of $F(x)$, for every $x \in \Omega$, and where $h_{X,\Omega}$ is the fill distance, see (9). In particular, the case $\|F \ominus Q^{\mathcal{M}}(F)\|_\infty := \|F \ominus Q^{\mathcal{M}}(F)\|_{C^0(\bar{\Omega})}$ should be taken care, that is with $\ell = 0$.

In the following remark, we survey two related bounds.

Remark 5.3. *Two known results in the spirit of (17) are worth mentioning. The first, from [17], uses embedding of F in a higher dimensional Euclidean space. It is shown that the quasi-interpolation in the manifold is converging to the linear quasi-interpolation of the Euclidean space. Then, for $F \in C^\alpha$, $l < \alpha$, and for any chart γ , it was shown that*

$$\left(\frac{d}{dx} \right)^l \left(\gamma \circ F - \gamma \circ Q^{\mathcal{M}}(F) \right) = \mathcal{O}(h^{\alpha-l}).$$

The second result is from [18] and develops the Taylor expansion of $G(x, y) = F(y) \ominus Q^{\mathcal{M}}(F)(x)$, which is in the tangent space of $Q^{\mathcal{M}}(F)(x)$. It then leads to a similar result with

$$d(F, Q^{\mathcal{M}}(F)) \leq C_Q \|F\|_{C^k} \sup_{1 \leq r \leq k} \sup_{x, y \in \Omega} \nabla_2^r F(y) \ominus Q^{\mathcal{M}}(F)(x) h^k,$$

where ∇^r is the covariant derivative of a bivariate function. Nevertheless, the multiscale proof assumes a stronger bound of the form (17).

5.4 Multiscaling of manifold-valued data

As in the Euclidean case, we will use the quasi-interpolation operators in a multiscale fashion to derive higher approximation capabilities and a dynamic framework for analyzing and processing data. We will now describe the scheme in more detail. First, we define the manifold scattered data version of quasi-interpolation and multiscale approximations. Then, we describe the assumptions needed and the resulted multiscale error bound.

Assume $X_1, X_2, \dots, X_L \subseteq \Omega$ is a sequence of discrete sets with more and more data sites. We choose support radii $\delta_1 > \delta_2 > \dots > \delta_L$, which should be proportional to the associated fill distances $h_1 > h_2 > \dots > h_L$ of the sets X_j . Then, for $k = 1, 2, \dots, L$ we compute local quasi-interpolants according to (15), that is

$$Q^{\mathcal{M}} \left(X_k, F|_{X_k} \right) (x) := \arg \min_{m^* \in \mathcal{M}} \sum_{x_j \in X_k} \Phi_k(x - x_j) d_{\mathcal{M}}(F(x_j), m^*)^2, \quad (18)$$

where $\Phi_k = \Phi_{\delta_k}$. However, as explained above, we will not apply these operators to the function itself but rather to the error function of the previous iteration. In the manifold setting, this requires some more preparation. Here, the multiscale method starts by setting a base manifold-valued function B . In algebraic settings, where \mathcal{M} is a Lie group, we can fix B to be the constant function with the identity element. Otherwise, we wish this function to be in the vicinity of the data. We can use, for example, a Voronoi tessellation with the samples $F|_{X_1}$. We set $F_0 = B$ and $e_0 = F \ominus B$. Then, we define for all $k = 1, 2, \dots, L$,

$$S_k = Q^{\mathcal{M}} \left(X_k, B|_{X_k} \oplus e_{k-1}|_{X_k} \right), \quad F_k = F_{k-1} \oplus (S_k \ominus B), \quad \text{and} \quad e_k = F \ominus F_k. \quad (19)$$

In the Euclidean case, this method reduces to the previously mentioned multiscale residual correction algorithm, as $+$, $-$ naturally replace \oplus and \ominus , respectively, and $B \equiv 0$ (the identity there).

Our next result implies that with a sufficiently accurate quasi-interpolation operator, the multiscale approximation error decays as we observed in the scalar case.

Corollary 5.4. *Let \mathcal{M} be a complete, open manifold. Then, under the condition of Theorem 4.1, its notation, and assumption (17), the following holds for all $F \in C^k(\bar{\Omega})$:*

$$\|F \ominus F_n\|_{\infty} \leq C_{0,k} (C_{k,k} \mu^k)^n \|F \ominus B\|_{C^k}. \quad (20)$$

6 Numerical examples

This section provides a numerical perspective to our multiscale study. First, we present some demonstrations of the multiscale scheme and then illustrate the numerical aspects of some of the theoretical findings we obtained. Finally we suggest an application to the scheme in anomaly detection. The entire source code is available as python implementation for reproducibility at the repository [6].

With $\phi_{d,k}$ we denote the compactly supported radial basis functions of minimal degree from [50] with indices d, k meaning that the RBF $\Phi = \phi_{d,k}(\|\cdot\|_2)$ is in $C^{2k}(\mathbb{R}^d)$ and is *positive definite* on \mathbb{R}^{ℓ} for $\ell \leq d$.

In what follows, we use the Wendland function $\phi_{3,1}$, see [47], to construct the quasi-interpolation kernel,

$$\phi(r) := \phi_{3,1}(r) = (1 - r)_+^4 (4r + 1). \quad (21)$$

To construct Q_X , we use ϕ as in Shepard's method, that is

$$Q_X(f)(x) = \sum_{x_i \in X} \frac{\phi(\|x - x_i\|_2) f(x_i)}{\sum_{x_j \in X} \phi(\|x - x_j\|_2)}, \quad x \in \Omega. \quad (22)$$

This method, by definition, reproduces constants, that is $Q_X(c)(x) = c$. We use Q_X for our multiscale approximation, but also as a reference approximation method. In the examples below, we refer to the quasi-interpolation approximation as “single scale”.

To evaluate error between a function f and its approximation at the j -th scale f_j , we use a discrete L_{∞} norm of the form:

$$\max_{x_i \in G(R,h)} |f(x_i) - f_j(x_i)|, \quad (23)$$

where $G(R, h)$ is a grid of points in the subdomain $R \subset \mathbb{R}^d$ with a fill distance h . Here, we use a rectangular $R \subset \mathbb{R}^2$ strictly inside Ω and $h = 0.02$ which is much finer than the sampling fill distance h_X . In the next examples, we compare each level of the multiscale to a single scale quasi-interpolation scheme with the same samples data having the same fill distance. All calculations are done in python using packages from [24, 44], and for plots we use [26].

6.1 A comparison between multiscale and single scale: the real-valued case

In this section we demonstrate the multiscale approximation and in particular its error rates, as shown in Theorem 4.1. We approximate real functions over \mathbb{R}^2 , and use samples over the domain $\Omega := [-0.95, 0.95]^2$ with a fill distance $h_X = 0.375$ and a scaling factor $\mu = 0.8$. The samples sites are generated from a Halton sequence [22]. For more details, see Appendix A.

We have approximated the following functions:

$$\begin{aligned} g(x, y) &= |\sin(4x) \cos(5y)|, \\ h(x, y) &= 5e^{-x^2 - y^2}. \end{aligned} \tag{24}$$

These functions present a different smoothness character, and we would like to test our multiscale approach for both. Thus, we conduct a comparison and provide the results in Figure 2. The left figures are graphical illustrations of the functions g and h . The right figures present the error decay. In particular, it shows that, in both cases, the error of the multiscale approximation decays faster than the error of the quasi-interpolation when using the same data.

We further investigate the function g , with emphasis on its non-smoothness. In Figure 3 we present the error maps for three levels: first, third and fifth. The error maps indicate not only the maximum value of error, as seen in Figure 2, but also how the error is distributed over the domain. Moreover, the figure illustrates how the multiscale error decays, particularly over smooth areas. Thus, the multiscale approach offers a tool for detecting non-smoothness. We continue exploring this attribute of the multiscale method in Section 6.4.

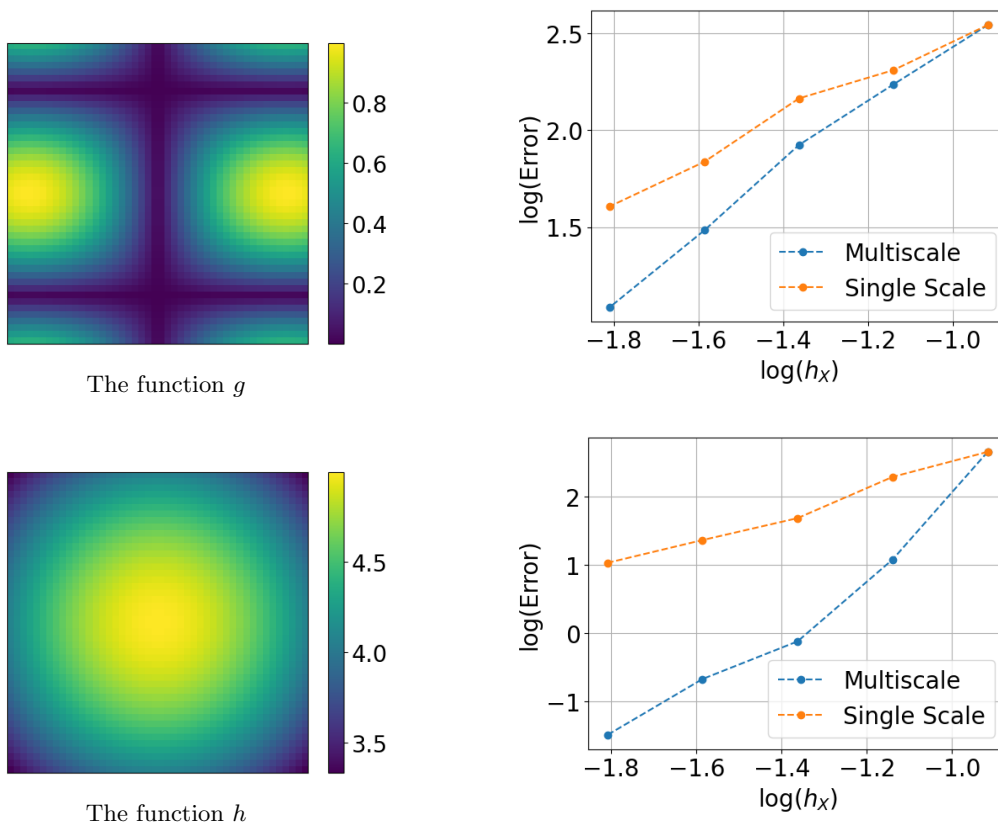


Figure 2: Error rates of the multiscale approximation versus the single scale approximation. On the left, the functions to be approximated, namely g and h of (24). On the right, their associated maximum deviation error, see (23), given in a log-log plot as a function of the fill distance, see (9).

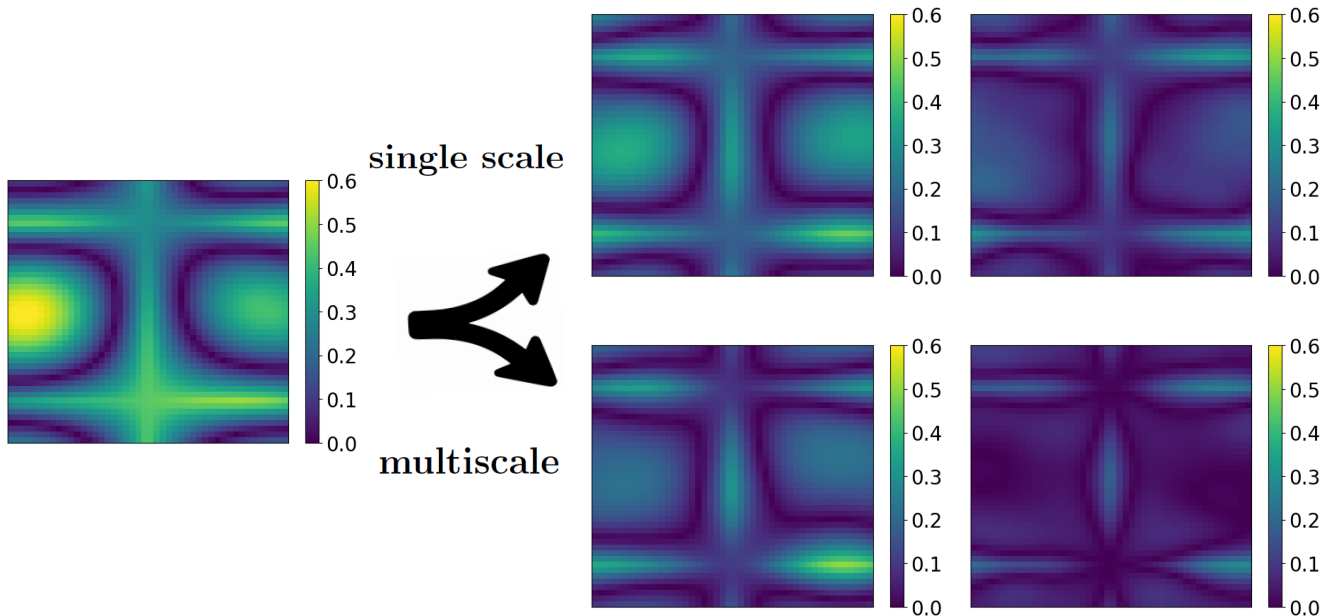


Figure 3: Comparing the error maps: the absolute deviation error when approximating g of (24) over three different levels of data densities. The first coarse level, on the left, is the basis of the multiscale method and thus yields the same approximation for both methods. Then, in the middle, we show the third level where the multiscale error appears below the single scale one. Finally, we provide the fifth, most fine approximation level on the right. Note how the multiscale approach presents a more rapid error decay around smoother areas of the function.

6.2 Validating our analysis

In this part, we numerically validate several of our theoretical findings concerning quasi-interpolation (Corollary 3.3) and multiscale approximation (Theorem 4.1). The function we approximate is:

$$f(x, y) = \sin(2x + 1) \cos(3y + 1.5). \quad (25)$$

Here, we continue to use $\phi_{3,1}$ as above and the data sites X are grids with the same fill distance and size as the sampling grids before.

6.2.1 The effect of polynomial reproduction's degree

The following experiment shows how the degree of polynomial reproduction affects the convergence order of quasi-interpolation. We approximate f of (25) with Q_X of (4) and specifically use Q_X with constant reproduction as in (22), and then with another operator having quadratic polynomial reproduction. We obtain higher-degree polynomial reproduction by using the moving least-squares method from [49]. The output of this comparison is given in Figure 4 and shows that the quasi-interpolation operator with quadratic polynomial reproduction has a better error decay than the one with constant polynomial reproduction, as one may expect. We now continue to examine this difference further.

We validate (11) of Corollary 3.3 for the two cases of polynomial reproduction degrees. Applying logarithm on (11) gives

$$\log \|f - Q_X(f)\|_{C^0(\bar{\Omega})} \leq \log C_{m+1,0} \|f\|_{C^{m+1}(\bar{\Omega})} + (m+1) \log h_{X,\Omega}, \quad (26)$$

Recall that we obtain $m+1 = 1$ in the constant reproduction case, and $m+1 = 3$ in the quadratic reproduction case.

Fitting the results of Figure 4 to (26) gives slope values of 1.92 for the constant reproduction and 3.04 to the quadratic reproduction. Note that the corollary guarantees minimal slopes of 1, 3, respectively.

Remark 6.1. *Constructing Q_X with polynomial reproduction degree greater than 0 usually involves solving linear systems, as in (7). Typically, these linear systems tend to be ill-conditioned. For instance, most of the systems we solved for the quadratic case had condition numbers greater than 10^4 . Henceforth, we focus on Shepard's method. We show further investigation of this insight in Section 6.3.*

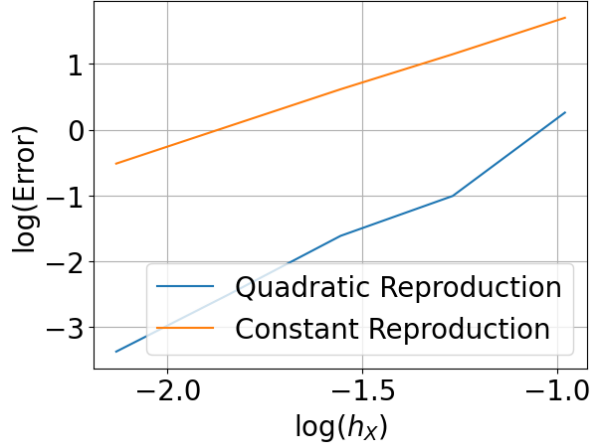


Figure 4: Comparison between error decay rates under constant reproduction and quadratic reproduction quasi-interpolants.

6.2.2 Revealing key parameters

This part investigates two of the main parameters of the multiscale method: the number of iterations, which we denote by j , and the scaling factor μ . In particular, we test numerically Theorem 4.1, by observing the error decay as a function of the iterations j via a log simplification of (12):

$$\log \|f_j - f\|_\infty \leq \log C_{0,k} \|f\|_{C^k(\bar{\Omega})} + j \log (C_{k,k} \mu^k). \quad (27)$$

Here, since we use constant reproduction quasi-interpolation, we have $k = 1$.

First, we set three fixed values of μ and apply our multiscale approximation for each one. Then, we calculate the slopes of each experiment when fitting a linear connection between the log of the approximation error and j , as in (27). The results are depicted in the upper row of Figure 5 and indicate that the relation is indeed close to be linear as in the bound we obtained.

In (27), the slope of the above linear connection is

$$\log C_{k,k} + k \log \mu. \quad (28)$$

Recall that in order to guarantee convergence we must have $C_{k,k} \mu^k < 1$. Therefore, to estimate this crucial quantity, we reuse the above results and for each j we draw the average slope as a function of $\log(\mu)$. Finally, we use a linear regression to extract from the slopes and (28) the parameters $\log C_{1,1}$ and k . The bottom plot of Figure 5 shows this linear fit, where we get $\log C_{1,1} = -0.42$ and thus $C_{1,1} = 0.66$. This value promises convergence for the μ values we used for the test. In addition, we have $k = 2.47$, which is much better than theoretical bound of 1.

6.3 Obtaining quadratic rates with constant reproducing via multiscale

The advantage of Shepard's method with constant reproduction (22) lies in its simplicity, which results in an attractive complexity and preferred execution time comparing to higher degree reproduction schemes, see Remark 6.2 below. In this section, we show that the multiscale approach when using Shepard's operators can provide a comparable approximation result to a quasi-interpolation with a higher polynomial reproduction degree. Namely, one can achieve much-improved error decay by using multiscale while benefiting from the low computation load of Shepard's method.

For this example, we approximate the function g of (24) and use the same settings of approximation as in Section 6.1. The quadratic quasi-interpolation is the same as in Section 6.2.1. In Figure 6, we present the error decay of the multiscale and the single scale. The figure shows that the multiscale, which is based on reproducing constants, has a similar decay rate as the quasi-interpolation, which in turn is based on reproducing quadratics.

Remark 6.2. We briefly explain the complexity of quasi-interpolation for the above degrees of polynomial reproduction. First, to approximate $Q(f)$ at point x , we use data of points $x_i \in \text{supp } \phi_\delta(\|x - \cdot\|_2)$. These points are the neighbours of x as they satisfy $\|x - x_i\|_2 \leq \delta$, where δ is the support radius of ϕ_δ .

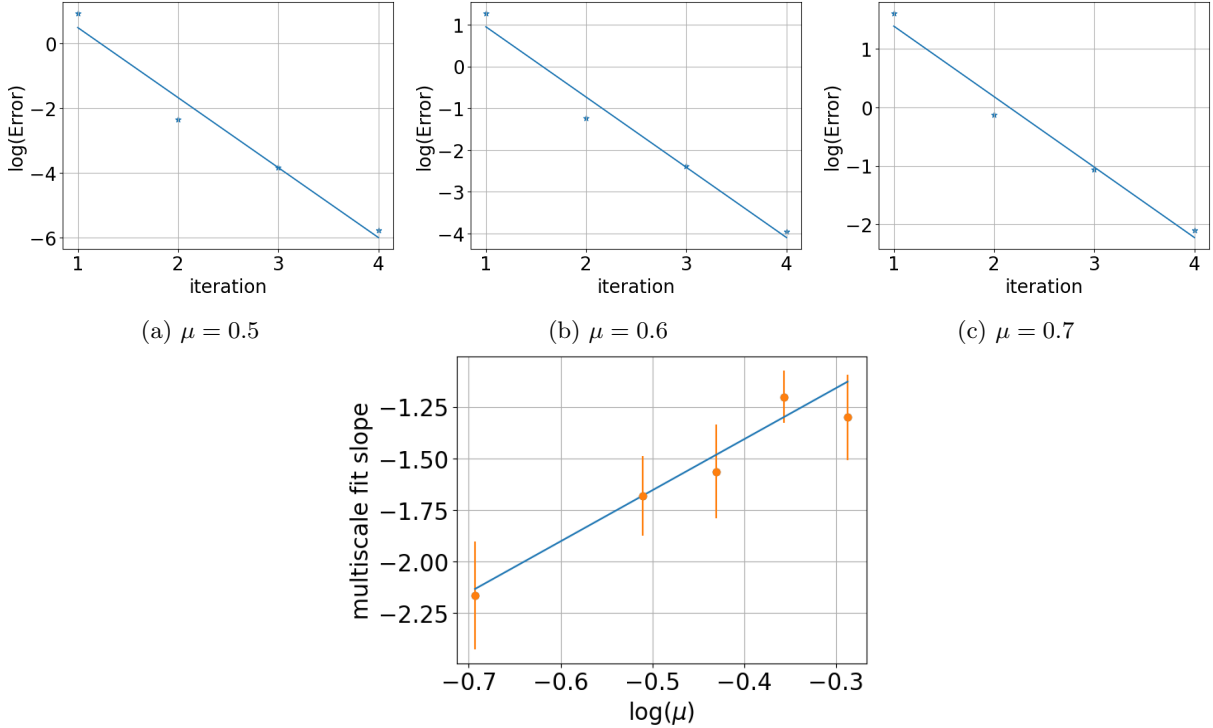


Figure 5: Exploring Theorem 4.1 via (27) as reflects by numerical tests: In the upper row, we show the approximation error as a function of the iterations and assign a slope value according to a linear fit. The bottom figure presents the connection between the slopes of each iteration and $\log(\mu)$ as in (28). The error bars are calculated from the different μ -s fits. The error of each slope is the standard deviation derived from the fitted parameters’ co-variance matrix. The result reveals the values $\log C_{1,1} = -0.42$ and $k = 2.47$. The latter is a larger value that the minimal guaranteed value of 1.

We organize the sites X in a k - d tree, with cost $O(dN \log N)$, where $N = \#X$, and d is the dimension of the domain. For a point x , a query of points in a radius δ , using the k - d tree, costs $O(\log N)$. Denote the complexity of weight calculation with ω . In constant reproduction $\omega = 1$. Else, in higher degree we solve a linear system meaning $\omega = Q^3(Q + \kappa)$, where $Q = \dim(\pi_m(\mathbb{R}^d)) = \binom{m+d}{d}$ (see, e.g., [50, Theorem 2.5]). Due to quasi-uniformity, for any δ there is a bound κ to the number of points in the δ -neighbourhood of x . So, finally, the complexity of the quasi-interpolation of a single point x is: $O(\log N + \omega\kappa)$.

6.4 Anomaly detection over scattered data by multiscale

When applying a local quasi-interpolation operator, the approximation error is related to the local smoothness of the approximated function. The multiscale method, when based on local quasi-interpolation uses several steps of local approximations thus provides a powerful tool to analyze the function’s local smoothness. In turn, this analysis mechanism shows efficiency when it comes to anomaly detection; see, for example, in [36]. We use this approach to detect anomalies based upon the approximation error of the multiscale method.

We demonstrate the above by approximating a function that we contaminate with a minor, synthetic anomaly. The approximated function is:

$$\tilde{f}(x, y) = \begin{cases} 1.01 \cdot f(x, y), & (x, y) \in [0.1, 0.25] \times [0.2, 0.4], \\ f(x, y), & \text{else,} \end{cases}$$

where f is from (25). The approximation’s configuration is the same as before, using Halton points as our scattered samples. We show in Figure 7 the fifth scale’s error distribution. Indeed it is easy to see that the anomaly region is easily detected using the multiscale’s error.

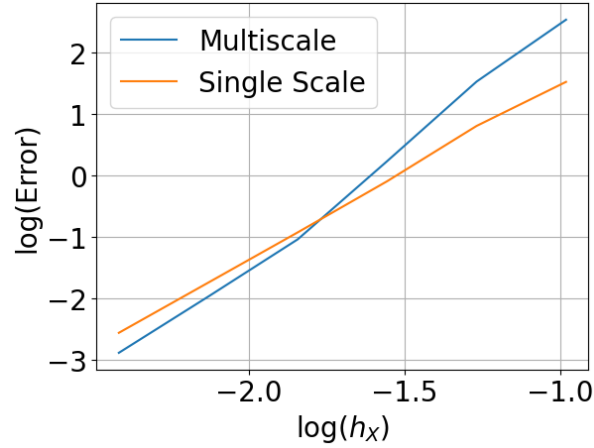


Figure 6: A comparison of error decay rates between constant reproduction multiscale and quadratic reproduction quasi-interpolation, when approximating the function g of (24).

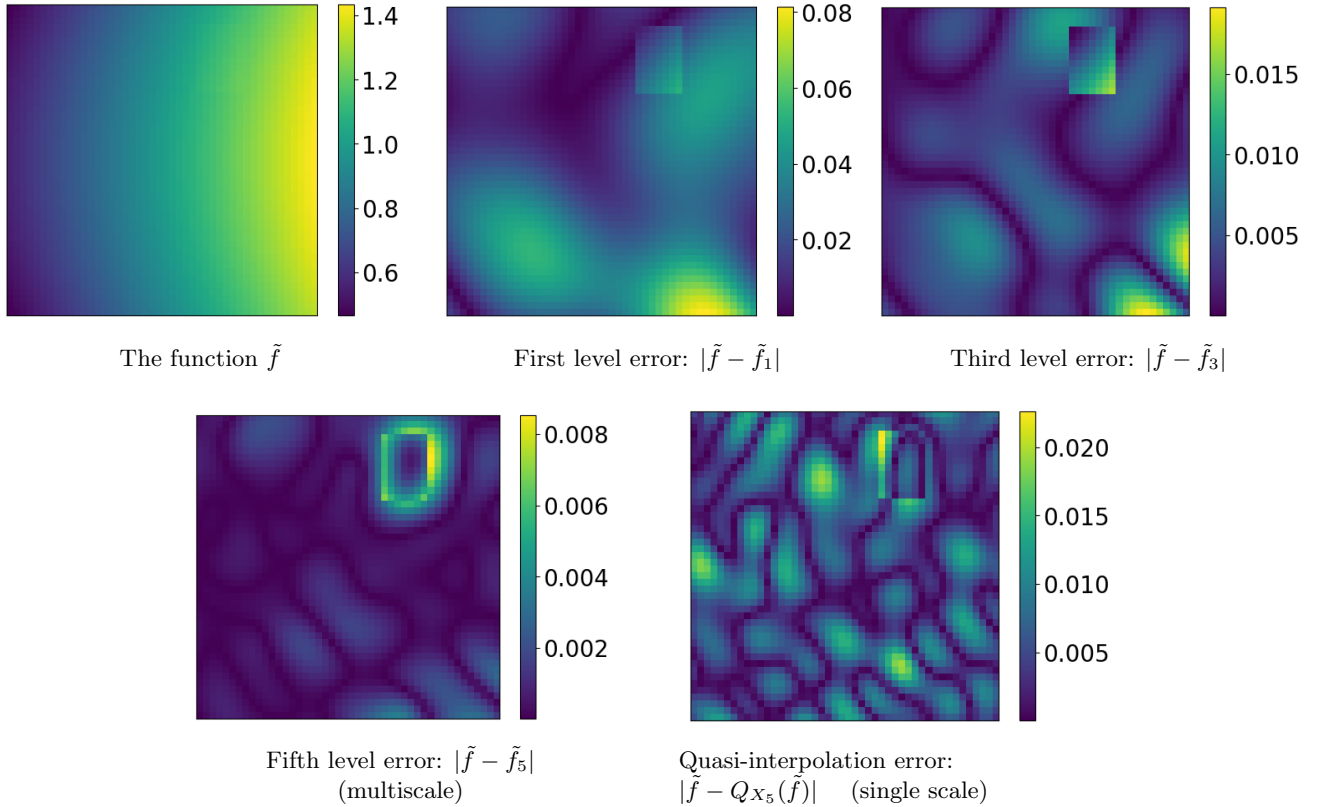


Figure 7: Anomaly detection using the multiscale approach. In the upper row, the function and two error maps correspond to the first and third levels of the multiscale. In the bottom row, the two error maps of the multiscale (left) and single scale of quasi-interpolation (right) correspond to the data of the fifth level. The anomaly is seen clearly through the multiscale error maps and especially over the last level. Detecting the same anomaly over the function (top left) or via the error map of the quasi-interpolation (bottom right) is much harder.

6.5 Scattered data approximation of manifold-valued functions

We demonstrate our multiscale analysis based on quasi-interpolation for functions defined on \mathbb{R}^2 and with values on $\text{SO}(3)$ (oriented rotations) and $\text{SPD}(3)$ (symmetric positive definite matrices). We use the quasi-interpolation of the form (15). The error between two functions F and H , analogous to (23), is

$$\max_{x_i \in G(R, h)} \rho(F(x_i), H(x_i)),$$

where the grid $G(R, h)$ has the same properties of the test grid in real valued scattered data.

6.5.1 Approximation over oriented preserving rotations

When evaluating (15), we required to calculate Karcher means. For that, we use an iterative process suggested in [37] and defined as,

$$Y_{j+1} = \text{Exp}_{Y_j} \left(\frac{\sum_{i=1}^N a_i \text{Log}_{Y_j}(F(x_i))}{\sum_{i=1}^N a_i} \right),$$

where Y_0 is set to be one of the values $F(x_i)$, and we stop iterating when $\rho(Y_{j+1}, Y_j) < \varepsilon$ for a predefined small tolerance $\varepsilon > 0$.

Here, we provide an example where we approximate a function over rotations. The function is defined as follows by the Euler angles, which are taken via the xyz convention:

$$F(x, y) = \text{Euler}_{xyz}(1.2 \sin 5x - 0.1, y^2/2 - \sin 3x, 1.5 \cos 2x). \quad (29)$$

In practice, we form the $\text{SO}(3)$ rotations from the Euler angles using the python package `scipy` [44]. We visualize the function by plotting the application of it, as field of transformations, on a fixed vector. This illustration appears at the most left image of Figure 8. As in previous examples, we compare our multiscale method with a direct application of the quasi-interpolation. The samples are scattered over our planer domain, as we demonstrate in the middle image of Figure 8. The comparison graph appears as the most right image of Figure 8, where we see how the multiscale error decays faster.

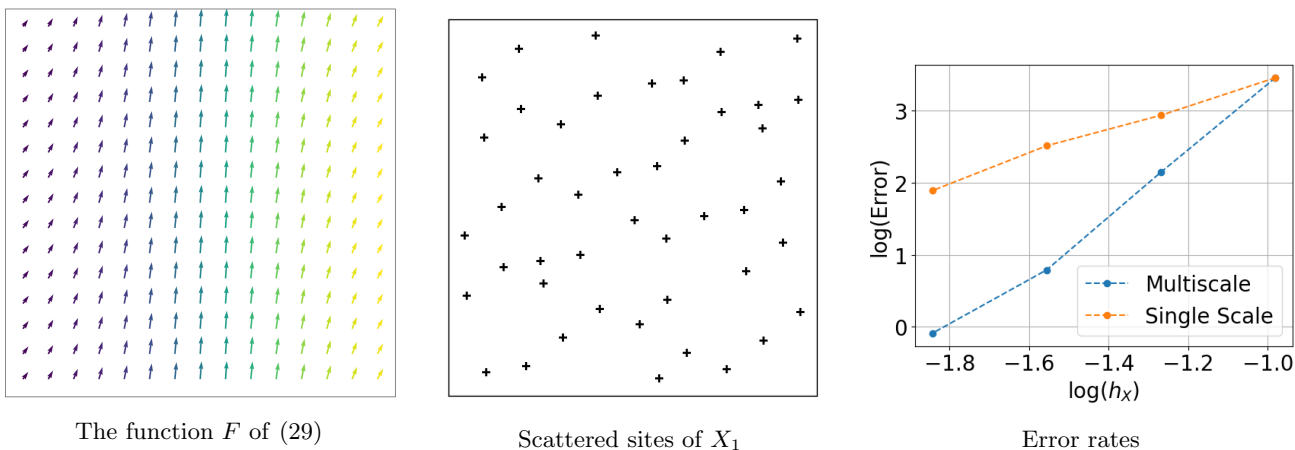


Figure 8: Comparison of approximating a field of rotations over a planar domain. The rotations in F are visualized by the effect of $F(x, y)$ on a fixed vector \hat{x} , where the color represents the z element $F(x, y)(\hat{x})_z$. The approximation sites are scattered at each level as a Halton sequence. On the left: the function to be approximated. In the middle: a demonstration of the scattered data sites of the first level. On the right: the approximation error rates.

6.5.2 Approximation over symmetric positive definite matrices

Recall that in $\text{SPD}(d)$, the exponential and logarithms get the symmetric form

$$\text{Log}_X(Y) = X^{1/2} \log(X^{-1/2} Y X^{-1/2}) X^{1/2}, \quad \text{Exp}_X(y) = X^{1/2} \exp(X^{-1/2} y X^{-1/2}) X^{1/2},$$

where \log and \exp are the standard matrix functions. Then, the geodesic distance is

$$\rho(X, Y) = \left\| \log \left(X^{-1/2} Y X^{-1/2} \right) \right\|_2,$$

To evaluate the Karcher means in the quasi-interpolation, we use iterations from [27] and define:

$$Y_{j+1} = \text{Exp}_{Y_j} \left(\theta_j \sum_{i=1}^N a_i \text{Log}_{Y_j} (F(x_i)) \right), \quad \theta_j = \frac{2}{\sum_{i=1}^N a_i(x) \frac{c_i^{(j)+1}}{c_i^{(j)}-1}},$$

where $c_i^{(j)}$ is the condition number of $Y_j^{-1/2} F(x_i) Y_j^{-1/2}$, and $Y_0 = \sum_{i=1}^N a_i F(x_i)$, which is a symmetric positive definite matrix as long as $a_i \geq 0$, which is the case for our Shepard's method (22).

In this example, we approximate a function F of SPD(3), of the form

$$F(x, y) = G(x, y) + (G(x, y))^T, \quad (30)$$

where $G(x, y) = (\cos 2y + 0.6) e^{-x^2-y^2} (5I + A) + I$, $A = \begin{pmatrix} \sin 5y & y & xy \\ 0 & 0 & y^2 \\ 0 & 0 & 0 \end{pmatrix}$. We use the representation of

any SPD matrix as a centred ellipsoid. This ellipsoid has main axes that are determined by the eigenvectors of the matrix and their lengths are the associated eigenvalues. Then, an illustration of F of (30) is given as the left image of Figure 9.

Again, we compare the error decay of the multiscale approximation versus the quasi-interpolation. The data sites were taken again, scattered as a Halton sequence and the error decay rates are provided in the right image of Figure 9. Also here, the multiscale's error decays faster.

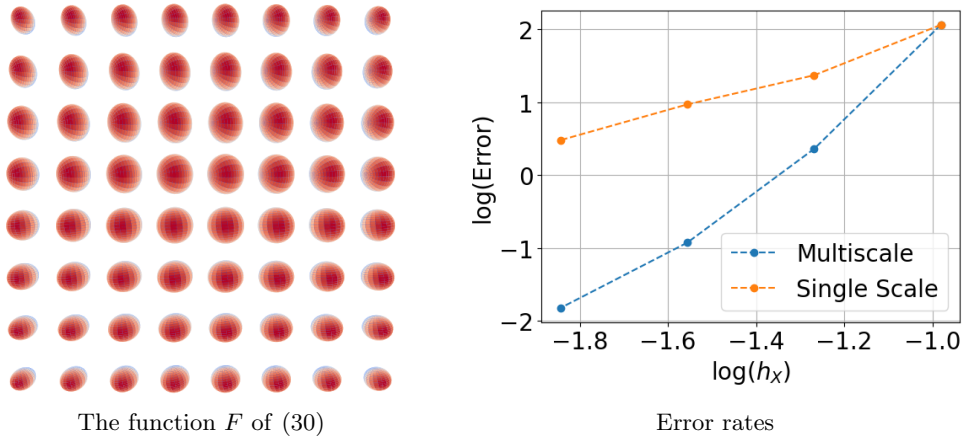


Figure 9: Comparison of approximating a field of SPD matrices over a planar domain. The matrices are visualized by their associated centered ellipsoids. The approximation sites are scattered at each level as a Halton sequence. On the left: the function to be approximated. On the right: the approximation error rates.

6.5.3 Application of denoising a field of rotations

We summarize the numerical section with an application of our manifold-valued scattered data approximation. This application is a denoising process where we use the multiscale error rates as indicators for noise removal. In particular, and as done in classical signal processing, we adopt a procedure where we diminish the levels of approximation where error drops below a fixed threshold.

In our example, we use the same field of rotation F of (29). Then, we contaminate the function by changing each value with its product against the exponential of a matrix which was sampled from a normal distribution with a fixed variance σ^2 . In other words, the random matrix is calculated in the Lie algebra and then projected back to the group. The samples are taken in a scattered-fashion from a Halton sequence

The denoising process starts after the first approximation level; then, we filter out from the sites set X_n all the sites with error larger than $t \cdot \max_{x \in X_n} \|F(x) \ominus F_{n-1}(x)\|$, where $0 \leq t \leq 1$ is a fixed threshold.

The first results of the above denoising process appear in Figure 10, where we present the error rates under various σ values. As the variance of the noise increases, the denoising procedure struggles, and the associated decay rates implicitly indicate that more noise is presented in the samples or that the function is less “smooth.” From several tests, we also learn that the denoising process is not sensitive to choosing different threshold values and in particular that all tested values between $0.75 \leq t \leq 0.95$ lead to similar results.

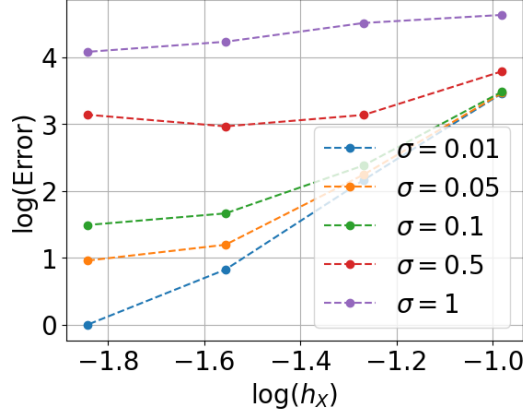


Figure 10: Approximation error rates, for our multiscale approximation, of fields of rotations contaminated with different levels of noise.

The visual result of the above denoising process appears in Figure 11, where we present the original function (left), its noisy version (middle), and our denoised approximation (right).

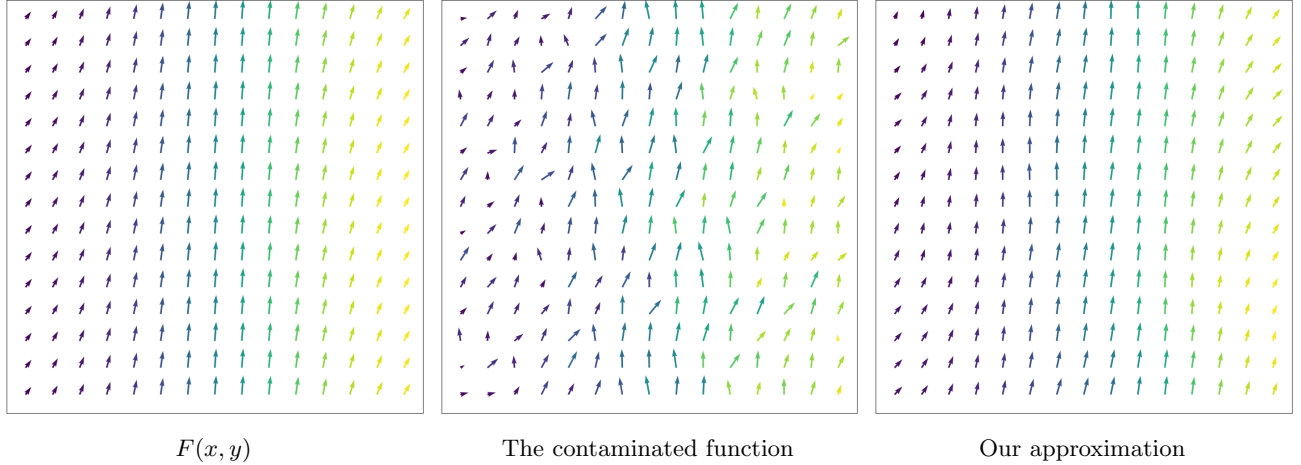


Figure 11: Visualization of $F(x, y)$ of (29) (left), its noisy version with variance of $\sigma = 0.2$ (middle) and the denoised approximation (right). The site picking is done with a threshold of $t = 0.9$.

Acknowledgments

We thank Nira Dyn for her contribution to this project’s conception and first steps. N. Sharon is partially supported by the NSF-BSF award 2019752.

References

- [1] David Amsallem, Julien Cortial, Kevin Carlberg, and Charbel Farhat. A method for interpolating on manifolds structural dynamics reduced-order models. *International journal for numerical methods in engineering*, 80(9):1241–1258, 2009.
- [2] Peter Benner, Serkan Gugercin, and Karen Willcox. A survey of projection-based model reduction methods for parametric dynamical systems. *SIAM review*, 57(4):483–531, 2015.
- [3] Sergio Blanes and Fernando Casas. *A concise introduction to geometric numerical integration*. CRC press, 2017.
- [4] Florent Bouchard, Jérôme Malick, and Marco Congedo. Riemannian optimization and approximate joint diagonalization for blind source separation. *IEEE Transactions on Signal Processing*, 66(8):2041–2054, 2018.
- [5] Ching Shyang Chen, Mahadevan Ganesh, Michael A Golberg, and AH-D Cheng. Multilevel compact radial functions based computational schemes for some elliptic problems. *Computers & Mathematics with Applications*, 43(3-5):359–378, 2002.
- [6] R. S. Cohen. <https://github.com/rafaels2/MultiscalteInterpolation>. yet to be published.
- [7] Carl de Boor. Quasiinterpolants and approximation power of multivariate splines. In *Computation of curves and surfaces*, pages 313–345. Springer, 1990.
- [8] Manfredo Perdigao Do Carmo and J Flaherty Francis. *Riemannian geometry*, volume 6. Springer, 1992.
- [9] Ramsay Dyer, Gert Vegter, and Mathijs Wintraecken. Barycentric coordinate neighbourhoods in Riemannian manifolds. *arXiv preprint arXiv:1606.01585*, 2016.
- [10] Nira Dyn and Nir Sharon. A global approach to the refinement of manifold data. *Mathematics of Computation*, 86(303):375–395, 2017.
- [11] Nira Dyn and Nir Sharon. Manifold-valued subdivision schemes based on geodesic inductive averaging. *Journal of Computational and Applied Mathematics*, 311:54–67, 2017.
- [12] Gregory E Fasshauer and Jack G Zhang. Iterated approximate moving least squares approximation. In *Advances in Meshfree Techniques*, pages 221–239. Springer, 2007.
- [13] Renzhong Feng and Feng Li. A shape-preserving quasi-interpolation operator satisfying quadratic polynomial reproduction property to scattered data. *Journal of computational and applied mathematics*, 225(2):594–601, 2009.
- [14] Michael S Floater and Armin Iske. Multistep scattered data interpolation using compactly supported radial basis functions. *Journal of Computational and Applied Mathematics*, 73(1-2):65–78, 1996.
- [15] T. Franz and H. Wendland. Multilevel quasi-interpolation. Preprint Bayreuth 2022, to appear in IMA Journal of Numerical Analysis, 2022.
- [16] QT Le Gia, Ian H Sloan, and Holger Wendland. Multiscale analysis in sobolev spaces on the sphere. *SIAM journal on numerical analysis*, 48(6):2065–2090, 2010.
- [17] Philipp Grohs. Quasi-interpolation in Riemannian manifolds. *IMA Journal of Numerical Analysis*, 33(3):849–874, 2013.
- [18] Philipp Grohs, Markus Sprecher, and Thomas Yu. Scattered manifold-valued data approximation. *Numerische Mathematik*, 135(4):987–1010, 2017.
- [19] Philipp Grohs and Johannes Wallner. Definability and stability of multiscale decompositions for manifold-valued data. *Journal of the Franklin Institute*, 349(5):1648–1664, 2012.
- [20] Karsten Grove and Hermann Karcher. How to conjugate 1-close group actions. *Mathematische Zeitschrift*, 132(1):11–20, 1973.

- [21] Mengwu Guo and Jan S Hesthaven. Reduced order modeling for nonlinear structural analysis using gaussian process regression. *Computer Methods in Applied Mechanics and Engineering*, 341:807–826, 2018.
- [22] John H Halton. On the efficiency of certain quasi-random sequences of points in evaluating multi-dimensional integrals. *Numerische Mathematik*, 2(1):84–90, 1960.
- [23] Hanne Hardering. *Intrinsic discretization error bounds for geodesic finite elements*. PhD thesis, FU Berlin, 2015.
- [24] Charles R. Harris, K. Jarrod Millman, Stéfan J van der Walt, Ralf Gommers, Pauli Virtanen, David Cournapeau, Eric Wieser, Julian Taylor, Sebastian Berg, Nathaniel J. Smith, Robert Kern, Matti Picus, Stephan Hoyer, Marten H. van Kerkwijk, Matthew Brett, Allan Haldane, Jaime Fernández del Río, Mark Wiebe, Pearu Peterson, Pierre Gérard-Marchant, Kevin Sheppard, Tyler Reddy, Warren Weckesser, Hameer Abbasi, Christoph Gohlke, and Travis E. Oliphant. Array programming with NumPy. *Nature*, 585:357–362, 2020.
- [25] Svenja Hüning and Johannes Wallner. Convergence analysis of subdivision processes on the sphere. *IMA Journal of Numerical Analysis*, 00:1–14, 2020. <https://doi.org/10.1093/imanum/draa086>.
- [26] John D Hunter. Matplotlib: A 2d graphics environment. *Computing in science & engineering*, 9(03):90–95, 2007.
- [27] Bruno Iannazzo, Ben Jeuris, and Filippo Pompili. The derivative of the matrix geometric mean with an application to the nonnegative decomposition of tensor grids. In *Structured Matrices in Numerical Linear Algebra*, pages 107–128. Springer, 2019.
- [28] Arieh Iserles, Hans Z Munthe-Kaas, Syvert P Nørsett, and Antonella Zanna. Lie-group methods. *Acta numerica*, 9:215–365, 2000.
- [29] Hermann Karcher. Riemannian center of mass and mollifier smoothing. *Communications on pure and applied mathematics*, 30(5):509–541, 1977.
- [30] Hermann Karcher. Riemannian center of mass and so called karcher mean. *arXiv preprint arXiv:1407.2087*, 2014.
- [31] Shoshichi Kobayashi and Katsumi Nomizu. *Foundations of differential geometry*, volume 1. John Wiley & Sons Inc, New York, 1963.
- [32] Quoc T Le Gia, Ian H Sloan, and Holger Wendland. Zooming from global to local: a multiscale rbf approach. *Advances in Computational Mathematics*, 43(3):581–606, 2017.
- [33] Quoc T Le Gia and Holger Wendland. Data compression on the sphere using multiscale radial basis function approximation. *Advances in Computational Mathematics*, 40(4):923–943, 2014.
- [34] Thuan Lieu, Charbel Farhat, and Michel Lesoinne. Reduced-order fluid/structure modeling of a complete aircraft configuration. *Computer methods in applied mechanics and engineering*, 195(41-43):5730–5742, 2006.
- [35] Leevan Ling. A univariate quasi-multiquadric interpolation with better smoothness. *Computers & Mathematics with Applications*, 48(5-6):897–912, 2004.
- [36] Stephane Mallat and Wen Liang Hwang. Singularity detection and processing with wavelets. *IEEE transactions on information theory*, 38(2):617–643, 1992.
- [37] Jonathan H Manton. A globally convergent numerical algorithm for computing the centre of mass on compact lie groups. In *ICARCV 2004 8th Control, Automation, Robotics and Vision Conference, 2004.*, volume 3, pages 2211–2216. IEEE, 2004.
- [38] Jens Markus Melenk. On approximation in meshless methods. In *Frontiers of numerical analysis*, pages 65–141. Springer, 2005.
- [39] Davoud Mirzaei. Analysis of moving least squares approximation revisited. *Journal of Computational and Applied Mathematics*, 282:237–250, 2015.
- [40] Alexander Petersen, Hans-Georg Müller, et al. Fréchet regression for random objects with Euclidean predictors. *The Annals of Statistics*, 47(2):691–719, 2019.

- [41] Inam Ur Rahman, Iddo Drori, Victoria C Stodden, David L Donoho, and Peter Schröder. Multiscale representations for manifold-valued data. *Multiscale Modeling & Simulation*, 4(4):1201–1232, 2005.
- [42] RR Rama and S Skatulla. Towards real-time modelling of passive and active behaviour of the human heart using podi-based model reduction. *Computers & Structures*, 2018.
- [43] Oliver Sander. Geodesic finite elements of higher order. *IMA Journal of Numerical Analysis*, 36(1):238–266, 2016.
- [44] Pauli Virtanen, Ralf Gommers, Travis E Oliphant, Matt Haberland, Tyler Reddy, David Cournapeau, Evgeni Burovski, Pearu Peterson, Warren Weckesser, Jonathan Bright, et al. Scipy 1.0: fundamental algorithms for scientific computing in python. *Nature methods*, 17(3):261–272, 2020.
- [45] Johannes Wallner and Nira Dyn. Convergence and C1 analysis of subdivision schemes on manifolds by proximity. *Computer Aided Geometric Design*, 22(7):593–622, 2005.
- [46] Ren-Hong Wang, Min Xu, and Qin Fang. A kind of improved univariate multiquadric quasi-interpolation operators. *Computers & mathematics with applications*, 59(1):451–456, 2010.
- [47] Holger Wendland. Piecewise polynomial, positive definite and compactly supported radial functions of minimal degree. *Advances in computational Mathematics*, 4(1):389–396, 1995.
- [48] Holger Wendland. Error estimates for interpolation by compactly supported radial basis functions of minimal degree. *Journal of approximation theory*, 93(2):258–272, 1998.
- [49] Holger Wendland. Local polynomial reproduction and moving least squares approximation. *IMA Journal of Numerical analysis*, 21(1):285–300, 2001.
- [50] Holger Wendland. *Scattered data approximation*, volume 17. Cambridge university press, 2004.
- [51] Holger Wendland. Multiscale analysis in sobolev spaces on bounded domains. *Numerische Mathematik*, 116(3):493–517, 2010.
- [52] Eleanor Wong, Jeffrey S Anderson, Brandon A Zielinski, and P Thomas Fletcher. Riemannian regression and classification models of brain networks applied to autism. In *International Workshop on Connectomics in Neuroimaging*, pages 78–87. Springer, 2018.
- [53] Alexander Zeilmann, Fabrizio Savarino, Stefania Petra, and Christoph Schnörr. Geometric numerical integration of the assignment flow. *Inverse Problems*, 36(3):034003, 2020.

A Implementation details of scattered data

Our approximation is local and requires data from nearby sites. This is a result of using a local quasi-interpolation and it offers many advantages. When the sites (the function samples in the parameter space) are on a grid, it is easy to find the closest points just by indices calculation. However, when working with scattered points, finding the nearest points requires special attention.

To generate sites for our examples, we choose to use Halton sequence [22]. Specifically, the Halton sequence is constructed using coprime numbers as its bases, where we use the bases 2, 3. As our basic set, we generate such a Halton sequence with $n = 400$ points and denote it by $H_{2,3}(400)$. Then, we scale and duplicate the sites, while keeping the ratio between the fill distance and the separation radius (see (9)) fixed as $h_X/q_X = 4.01$. Next, we scale it with $r = h_X/h_{H_{2,3}(400)}$, where h_X is the requested fill distance. To fill a given domain Ω , we cover it with translates to obtaining

$$X = \bigcup_{i=0}^{\lceil \frac{x_{\max} - x_{\min}}{r} \rceil} \bigcup_{j=0}^{\lceil \frac{y_{\max} - y_{\min}}{r} \rceil} \left\{ rH_{2,3}(400) + (x_{\min} + ri, y_{\min} + rj) \right\} .$$

We show an example for such a set of scattered points in Figure 12.

Afterward, when the data sequence is generated, we use *k-d trees* as the data structure for the scattered locations. In practice, our implementation utilizes the package *pykdtree* for querying nearest neighbors within the RBF’s support. Its theoretical performance is discussed in [50, Section 14.2].

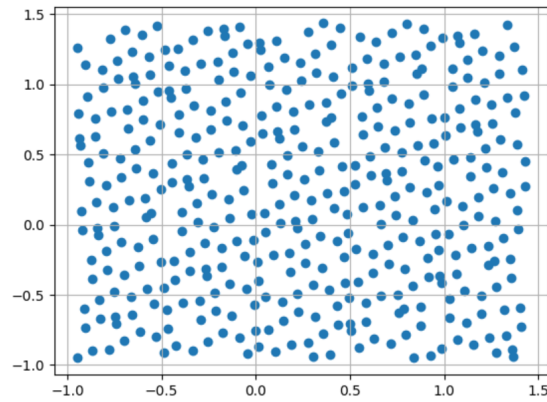


Figure 12: Halton points with $h_X = 0.158$, which is equivalent to the fourth scale in our examples.